Optics Letters

Patterned graphene edges for tailored reflection of plasmonic modes

GILLES ROSOLEN* AND BJORN MAES

Micro- and Nanophotonic Materials Group, University of Mons, Place du Parc 20, 7000 Mons, Belgium
**Corresponding author: gilles.rosolen@umons.ac.be*

Received 12 May 2015; accepted 18 May 2015; posted 21 May 2015 (Doc. ID 240749); published 5 June 2015

Combining graphene with plasmonics is expected to lead to new nanoscale applications such as sensors, photodetectors, and optical circuits, since graphene plasmons in the infrared have relatively low losses and are easily tunable. It was shown that the edges of a graphene sheet completely reflect these plasmons with negligible radiation losses. Here, however, we examine structured graphene edges, which provide the ability to tailor and even completely cancel the reflection. These properties depend on the suitable dimensions of the edge grating. We explain the reflection modulation via the appearance of longitudinal Fabry–Perot type modes. Interesting phase changes and resonances appear when the *longitudinal* modes interact with *lateral* modes mediated by edge plasmons.

OCIS codes: (250.5403) Plasmonics; (050.2230) Fabry-Perot; (310.6860) Thin films, optical properties.

http://dx.doi.org/10.1364/OL.40.002727

Already known for its fascinating electron transport properties [1], graphene is also widely studied in photonics for strong light-mater interactions [2,3]. Although the optical properties are rather invariant in the visible range (a constant 2.3% of the light is absorbed [4]), they are very suitable for applications in the infrared range [5]. At these frequencies graphene sustains plasmons, which are collective oscillations of electrons that confine electromagnetic waves to deeply sub-wavelength regimes. Compared to noble-metal plasmons (or plasmon polaritons), graphene plasmons (GPs) are considered more strongly confined and propagate over a relatively longer distance [6].

A most interesting feature of these plasmons is that their properties are easily tunable via electrostatic doping of the graphene sheet [7,8]. This is a windfall for plasmonic circuitry invented to overcome photonic downscaling and integration problems [9]. Novel circuits using GPs are now under active investigation [10–14]. The strong confinement and high sensitivity to the environment also finds applications for nanosensors [15,16] or modulators [17,18]. Furthermore, GPs were studied in nano-resonators with ribbons [19,20] and antennas [21].

Moreover, GPs were experimentally mapped in tip-shaped graphene sheets [22,23]. A near-total reflection of GPs at the edge of the sheet, with negligible radiation losses, was observed. Precise theoretical studies indicated a nontrivial phase shift upon reflection of $\varphi_r = 0.85$ rad [24] (with $e^{-j\varphi_r}$ convention), largely independent on wavelength and doping level.

Here we numerically show that a patterned graphene edge can strongly tailor and even completely cancel the reflection, in strong contrast with the unpatterned edge. We demonstrate that this modulation arises from coupling with Fabry–Perot cavities formed by ribbon GPs in the longitudinal direction. Interesting features appear when there is interaction with lateral resonances via edge modes [19]. A strong coupling with these edge modes at patterned interfaces needs to be considered for graphene infrared applications.

The particular pattern we study (Fig. 1) is a grating in a semi-infinite free-standing sheet in air, that is described as a ribbon array with elements of length l, width w, and period p. This can be experimentally realized via chemical vapor deposition [22] or electron-beam lithography [25]. The grating is excited via an in-plane GP, perpendicular to the edge (incidence along y-axis, Fig. 1).

For this problem, full 3D calculations are needed, which we performed with COMSOL, a commercial finite element-based software package. A single period is simulated, delimited by perfect magnetic boundaries in the x-direction, with Perfectly Matched Layers on the z- and y-boundaries in order to account for radiation losses. Graphene optical properties are defined by the Kubo Formula [26,27] at free-space wavelength $\lambda_0 = 10$ μm, with doping level $E_F = 1$ eV and scattering lifetime of electrons $\tau_g = 0.16$ ps. The graphene permittivity for an effective thickness of $t = 2$ nm is then $\varepsilon = -185 - 6.4i$ (a typical approach to accurately model the very thin sheet), and the corresponding plasmon effective wavelength is $\lambda_p = 1.16$ μm.

Note that the results are very similar for a different doping and wavelength if the structural parameters are scaled with the plasmon wavelength of the graphene sheet, so the conclusions are more general.

The reflectance of an in-plane plasmon mode perpendicularly incident on the grating constitutes our main result (Fig. 2), as we observe a rich characteristic in function of the ribbon length l (normalized to λ_p) and width w (normalized to

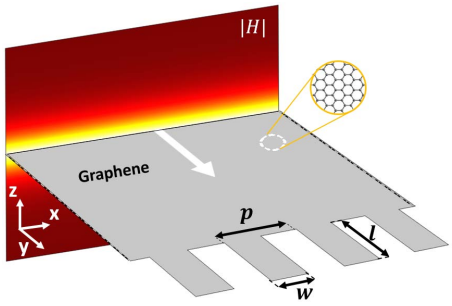

Fig. 1. Patterned edge on a graphene sheet, with period p, length l, and width w. The norm of the incident graphene plasmon magnetic H-field is depicted in the background.

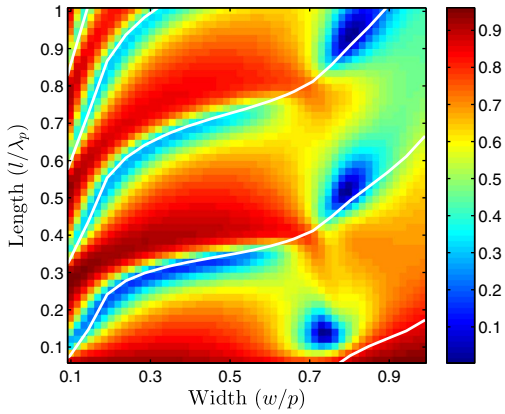

Fig. 2. Reflectance of a GP impinging the patterned edge as a function of normalized ribbon width w/p and length l/λ_p. Theoretical Fabry–Perot modes depicted with white lines.

the period p). The reflectance here is the power returned into the counter-propagating plasmon mode (excluding the losses in the incident section), as we fixed $p = 0.95\lambda_p$, so there is no diffraction toward other directions. If the graphene edge was unstructured, it would give total reflectance, whereas now zones with near-zero reflectance appear (blue zones), which means near-complete absorption as the radiation losses remain very small. In the following we explain these features through models that are as compact as possible.

The considered structure (Fig. 1) can be viewed as a graphene sheet connected with a finite graphene ribbon grating (GRG) of length l. The reflectance dips appear when the plasmon is trapped in the grating: a GRG mode is reflected back and forth with internally constructive interference. This Fabry–Perot (FP) resonance condition is

$$2\Re\{\beta\}l + \varphi_{r_{21}} + \varphi_{r_{23}} = 2m\pi, \quad \textbf{(1)}$$

where $\Re\{\beta\}$ is the real part of the propagation constant of the (fundamental and only) GRG plasmonic mode, $\varphi_{r_{21}}$ and $\varphi_{r_{23}}$ are the reflection phases for the fundamental mode at the two different interfaces of the GRG cavity, and m is an integer. Upon calculating $\Re\{\beta\}$, $\varphi_{r_{21}}$, and $\varphi_{r_{23}}$ (through separate simulations), we can represent the first three orders with white lines in Fig. 2. The single-mode description agrees well with the full-structure simulation results, with deviations mainly for widths $w > 0.7p$ that increase for smaller lengths l. Indeed, at the interfaces, evanescent modes are generated (similar to metallic edges [28]), and they are expected to have a larger influence for short cavities (small l) and larger w (better match with edge mode, discussed below). Note that the complex modal reflection (or transmission) is written following the convention $r_{ij} = \sqrt{R_{ij}}e^{-j\varphi_{r_{ij}}}$.

We are now in a position to analyze the behavior of the resonances in more detail, using as few parameters as possible, amongst others via the parameters of Eq. (1). Figure 3(a) represents the real part of the effective refractive index ($\Re\{n_{\text{eff}}\}$) of the fundamental GRG mode (blue line) as a function of the ribbon width w (where $\beta = 2\pi n_{\text{eff}}/\lambda_0$). This mode (which builds up the resonance in the GRG) is highly confined (large n_{eff}) for narrow ribbons, while for wider ribbons, the mode ultimately reaches the index of a pristine graphene sheet plasmon (red dashed line). If not embedded in a grating (single ribbon, black dashed line), the dispersion of the fundamental mode approaches the edge mode dispersion (green dashed line). Note that they dissociate at $w \approx 0.7p$ when the ribbon modes in the GRG start to interact with their neighbors via the edge modes (edge mode and GRG dispersion crossing). These edge modes will play an important role in our description.

The phases in Eq. (1) have a direct influence on the modelled resonances (white lines in Fig. 2). Figure 3(b) represents the reflection and transmission phases of the GRG plasmon at the interfaces of the FP cavity, see Fig. 3(c) for their definitions. Figure 3(b) shows two regions where the phases rapidly change ($w/p < 0.2$ and $w/p > 0.7$). These fast changes are responsible for the slope variations of the FP resonances (blue regions, Fig. 2), also explicit in the single-mode model (white lines, Fig. 2). They are both connected to a strong coupling with lateral (x-direction) FP resonances via edge modes (discussed below). The variation in the reflection phase [29] of the GRG at $w = 0.75p$ ($\varphi_{r_{23}}$) characterizes another lateral FP-cavity resonance at the end of the GRG (into air, see below). Note that $\varphi_{r_{23}}$ tends to the value 0.85 rad for a straight edge ($w/p = 1$).

Finally, Fig. 3(d) shows the transmittance and reflectance from GRG to a graphene sheet (T_{21} and R_{21}) and the reflectance at the end of the grating (R_{23}), see Fig. 3(c). By reciprocity $T_{12} = T_{21}$, so T_{21} (red line) also applies for transmittance from graphene sheet to GRG.

We also calculated the average of the magnetic field z-component at the lateral edges of the sheet-grating interface [Fig. 3(d), green-dot line, right axis]. At this interface only part of the energy stays in the y-directed longitudinally propagating modes ($R_{21} + T_{21} < 1$). With negligible radiation losses and without other longitudinally propagating modes, the remaining energy flows toward evanescent modes, determined as $c_e = 1 - R_{21} - T_{21}$ [green line, Fig. 3(d)]. The evanescent contribution c_e mainly corresponds to the edge mode, propagating in the lateral x-direction [19] [sketched in Fig. 3(c)]. This is correlated with the averaged edge magnetic field [green line and dots in Fig. 3(d)]: two peaks are observed at $w = 0.15p$ and $0.7p$. The corresponding electric fields are represented in Figs. 4(a) and 4(b) and they indicate a third-order and a first-order lateral FP resonance along the edge, respectively. Accordingly, the Poynting vectors [green arrows, Figs. 4(a) and 4(b)] exhibit an enhanced energy flow along the x-direction edge. Note that the second-order resonance is not allowed by the symmetry of

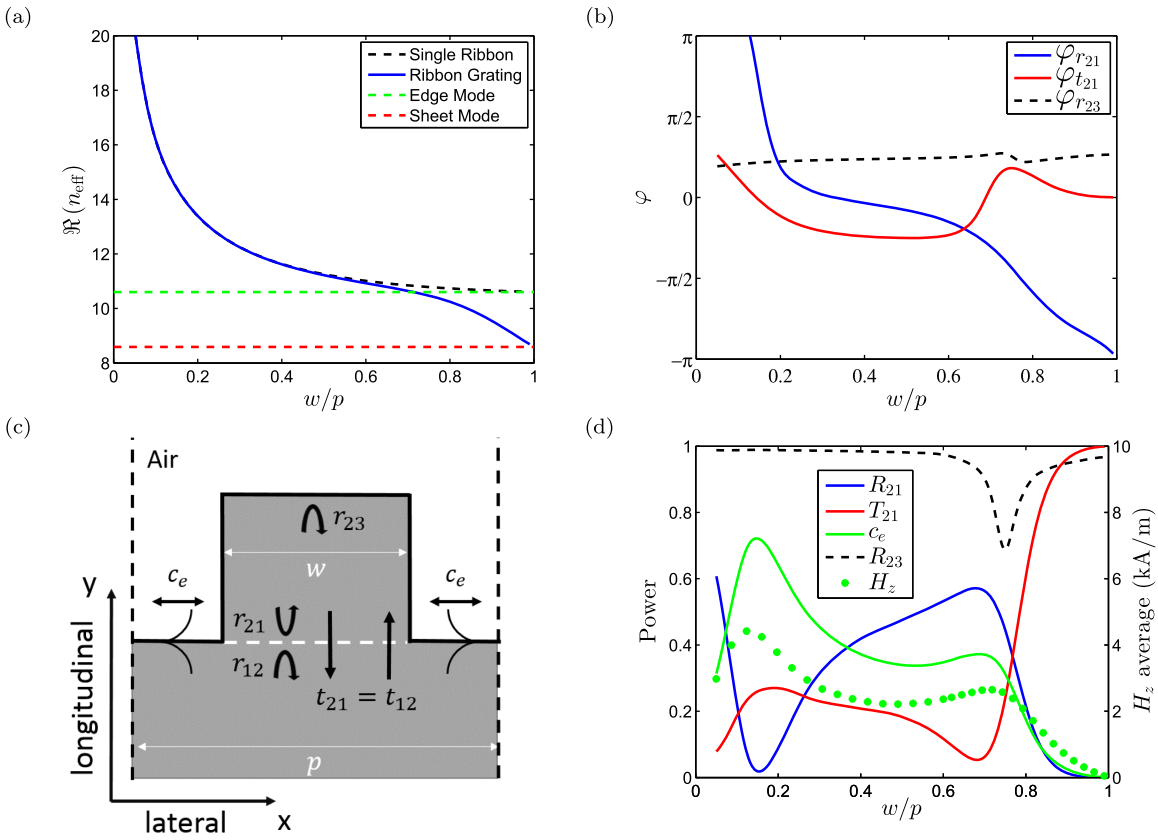

Fig. 3. (a) Dispersion of the relevant modes as a function of normalized width (w/p). (b) Reflection and transmission phase shift at the interfaces. (c) Top view with the relevant reflection and transmission parameters at the two interfaces. Lateral edge modes c_e are sketched. (d) Reflectance and transmittance at the two interfaces. c_e represents coupling with evanescent modes. The right axis shows the z-component magnetic field average at sheet-grating interface edge (dots).

the excitation. At the other end of the grating (to air), a similar edge mode lateral FP resonance at the end of the ribbons is responsible for the R_{23} reflectance dip around $w = 0.75p$ [black dashed line, Fig. 3(d)].

Now we have the elements to understand the complete structure. The first-order (lateral) resonance [Fig. 4(b)] is responsible for the disappearance of the (longitudinal) FP modes around $w = 0.7p$ in Fig. 2 (a band of higher reflectance appears, in between low reflectance zones). Indeed, in Fig. 3(d), the transmittance T_{21} falls to nearly zero, while edge mode coupling reaches 40%, which weakens the GRG cavity mode. Note that this particular width $w = 0.7p$ corresponds with the crossing point of the edge mode and the grating ribbon dispersion [Fig. 3(a)].

The other lateral edge mode resonance [peak around $w = 0.15p$ in Fig. 3(d)], however, does not spoil the reflectance dip in Fig. 2 at $w = 0.15p$. This is understood considering that the transmittance $T_{12} = T_{21}$ is not affected in this case [red line in Fig. 3(d)]. The altered parameters are the reflectance of the GRG plasmon R_{21} where a dip appears [blue line in Fig. 3(d)], and the slope of the phase $\varphi_{r_{21}}$ [blue line in Fig. 3(b)]. The latter influences the white line slopes in Fig. 2 for $w < 0.15p$.

Finally, we focus on the brutal changes of transmittance T_{21} and reflectance R_{21} when $w/p > 0.8$ [Fig. 3(d)]. At the final value ($w/p = 1$), the grating becomes a graphene sheet, leading to the absence of an interface, thus total transmittance and zero reflectance. Therefore, in this range, the losses remain fairly constant, while reflectance and transmittance change very rapidly. This leads to a particular value of w/p that achieves critical coupling (losses equal coupling), whereas the other values are under- or overcoupled. This explains the localized minima (tight blue spots in Fig. 2) in this regime, in contrast to the more extended FP resonances for $w/p < 0.8$ (elongated blue minima zones).

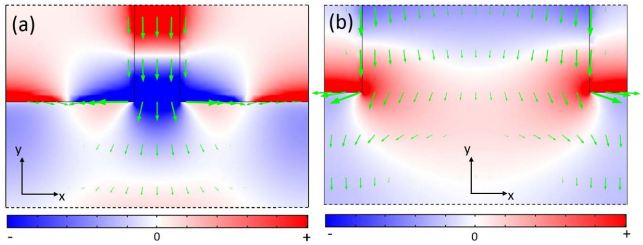

Fig. 4. Top view of the graphene sheet with the real part of the y-component of the electric field for (a) $w = 0.15p$ and (b) $w = 0.7p$, corresponding to lateral (x-direction) FP resonances of the edge mode. The excitation comes from the top via a semi-infinite GRG and is transmitted to a semi-infinite graphene sheet at the bottom. Poynting vectors are sketched in green arrows, with the arrow length depicting the vector norm in logarithmic scale.

We conclude that plasmon reflectance at the edge of a graphene sheet is profoundly influenced by its shape. The examined ribbon grating case offers longitudinal and lateral edge-mode Fabry–Perot resonances that drastically decrease the reflection for particular ribbon length and width combinations, where it would have been nearly 100% for a nonstructured edge. The edge mode coupling is associated with phase changes, influencing the positions of the longitudinal cavity modes. Furthermore, the rapidly changing transmittance beyond such a resonance leads to particular points of critical and near-zero reflection. These results are useful for the design of nano-optical circuitry, sensors, and antennas that employ graphene plasmons.

Belgian Science Policy Office (BELSPO) "Photonics@be" (P7-35); Fonds De La Recherche Scientifique—FNRS (Belgian National Fund for Scientific Research).

REFERENCES

1. A. Castro Neto, F. Guinea, N. M. R. Peres, K. Novoselov, and A. K. Geim, Rev. Mod. Phys. **81**, 109 (2009).
2. A. N. Grigorenko, M. Polini, and K. Novoselov, Nat. Photonics **6**, 749 (2012).
3. F. Bonaccorso, Z. Sun, and A. Ferrari, Nat. Photonics **4**, 611 (2010).
4. R. Nair, P. Blake, A. N. Grigorenko, K. Novoselov, T. Booth, T. Stauber, N. M. R. Peres, and A. Geim, Science **320**, 1308 (2008).
5. T. Low and P. Avouris, ACS Nano **8**, 1086 (2014).
6. M. Jablan, H. Buljan, and M. Soljacic, Phys. Rev. B **80**, 245435 (2009).
7. Z. Q. Li, E. A. Henriksen, Z. Jiang, Z. Hao, M. C. Martin, P. Kim, H. Stormer, and D. N. Basov, Nat. Phys. **4**, 532 (2008).
8. A. Vakil and N. Engheta, Science **332**, 1291 (2011).
9. T. Ebbesen, C. Genet, and S. Bozhevolnyi, Phys. Today **61**(5), 44 (2008).
10. J. L. Garcia-Pomar, A. Y. Nikitin, and L. Martin-Moreno, ACS Nano **7**, 4988 (2013).
11. G. Rosolen and B. Maes, J. Opt. **17**, 015002 (2015).
12. W. Lu, W. Zhu, H. Xu, Z. Ni, Z. H. Dong, and T. Cui, Opt. Express **21**, 186757 (2013).
13. X. Zhu, W. Yan, N. Asger Mortensen, and S. Xiao, Opt. Express **21**, 3486 (2013).
14. B. Wang, X. Zhang, X. Yuan, and J. Teng, Appl. Phys. Lett. **100**, 131111 (2012).
15. K. S. Novoselov, V. I. Falko, L. Colombo, P. R. Gellert, M. G. Schwab, and K. Kim, Nature **490**, 192 (2012).
16. Q. He, S. Wu, Z. Yin, and H. Zhang, Chem. Sci. **3**, 1764 (2012).
17. B. Sensale-Rodriguez, R. Yan, M. Kelly, T. Fang, K. Tahy, W. Hwang, D. Jena, L. Liu, and H. Xing, Nat. Commun. **3**, 780 (2012).
18. Z. Li and N. Yu, Appl. Phys. Lett. **102**, 131108 (2013).
19. A. Y. Nikitin, F. Guinea, F. J. Garcia-Vidal, and L. Martin-Moreno, Phys. Rev. B **84**, 161407 (2011).
20. S. Thongrattanasiri, I. Silveiro, and F. Javier Garca de Abajo, Appl. Phys. Lett. **100**, 201105 (2012).
21. I. Llatser, C. Kremers, A. Cabellos-Aparicio, J. M. Jornet, E. Alarcon, and D. N. Chigrin, Photon. Nanostr. Fundam. Appl. **10**, 353 (2012).
22. J. Chen, M. Badioli, P. Alonso-Gonzalez, S. Thongrattanasiri, F. Huth, J. Osmond, M. Spasenovoc, A. Centeno, A. Pesquera, P. Godignon, A. Z. Elorza, N. Camara, F. Garcia de Abajo, R. Hillenbrand, and F. H. L. Koppens, Nature **487**, 77 (2012).
23. Z. Fei, A. S. Rodin, G. O. Andreev, W. Bao, A. S. McLeod, M. Wagner, L. M. Zhang, Z. Zhao, M. Thiemens, G. Dominguez, M. M. Fogler, A. H. C. Neto, C. N. Lau, F. Keilmann, and D. N. Basov, Nature **487**, 82 (2012).
24. A. Y. Nikitin, T. Low, and L. Martin-Moreno, Phys. Rev. B **90**, 041407 (2014).
25. Z. Fang, S. Thongrattanasiri, A. Schlather, Z. Liu, L. Ma, Y. Wang, P. M. Ajayan, P. Nordlander, N. J. Halas, and F. J. Garcia de Abajo, ACS Nano **7**, 2388 (2013).
26. L. Falkovsky and A. Varlamov, Eur. Phys. J. B **56**, 281 (2007).
27. L. Falkovsky, J. Phys. **129**, 1 (2008).
28. P. Lalanne and J. P. Hugonin, Nat. Phys. **2**, 551 (2006).
29. B. J. J. Slagmolen, M. B. Gray, K. G. Baigent, and D. E. McClelland, Appl. Opt. **39**, 3638 (2000).